

Cite this: *RSC Adv.*, 2015, 5, 65100

# Remarkable capacitive enhancement of templated carbon materials by the redox additive electrolyte of *p*-phenylenediamine†

Yong Fu Nie,<sup>‡a</sup> Qian Wang,<sup>‡a</sup> Hai Tao Yi,<sup>a</sup> Xiang Ying Chen<sup>\*a</sup> and Zhong Jie Zhang<sup>\*b</sup>

Nanoporous carbon materials with hierarchical porosities have been produced *via* a template carbonization method, in which potassium citrate (or gelatin) serves as the carbon precursor and Mg(OH)<sub>2</sub> powder as the hard template. The P-3 : 1 sample derived from potassium citrate and Mg(OH)<sub>2</sub> (with a mass ratio of 3 : 1 at 800 °C) possesses high BET surface area of 1894.7 m<sup>2</sup> g<sup>-1</sup> and large total pore volume of 2.27 cm<sup>3</sup> g<sup>-1</sup>. To further improve the electrochemical performance, *p*-phenylenediamine (PPD, as redox-additive) of 5, 10, and 15 mmol L<sup>-1</sup> is introduced into the 6 mol L<sup>-1</sup> KOH as the mixed electrolyte, forming P-3 : 1-5/10/15 samples. Interestingly, the specific capacitances toward the P-3 : 1-5/10/15 samples have been greatly enhanced up to 579.2, 712.8 and 852.3 F g<sup>-1</sup> at 2 A g<sup>-1</sup>, respectively, which are greatly higher than that of 325 F g<sup>-1</sup> for the case of the pristine P-3 : 1 sample when measured at 6 mol L<sup>-1</sup> KOH electrolyte. Furthermore, the P-3 : 1-15 sample delivers high capacitance retention of 70.5% even after 5000 charge–discharge cycles. What's more, the synthesis method has been readily extended for the case of gelatin and Mg(OH)<sub>2</sub>, and a similar electrochemical trend in the cases of the P-3 : 1-5/10/15 samples also occurs.

Received 12th June 2015

Accepted 24th July 2015

DOI: 10.1039/c5ra11187k

www.rsc.org/advances

## 1. Introduction

In recent years, a simple and valid template carbonization method has been implemented for producing nanoporous carbon materials with high surface areas, well-controlled surface morphologies, hierarchical properties, and excellent electrochemical performance.<sup>1</sup> The templated carbon materials can be applied in wide areas of gas adsorption and diffusion behaviour,<sup>2</sup> electrodes for supercapacitors,<sup>3</sup> and energy storage devices.<sup>4,5</sup> In addition, nanoporous carbon materials can be achieved by removing templates or their decomposition products (if necessary) without further chemical or physical activation processes, and the method simplifies the preparation procedures. Some excellent examples concerning the template carbonization method are displayed as follows: Juan Balach *et al.* have produced targeted hierarchical nanoporous carbon materials with high specific surface area of 675 m<sup>2</sup> g<sup>-1</sup> and capacitance as high as 140 F g<sup>-1</sup>, in which cationic

polyelectrolyte serves as soft template.<sup>6</sup> Fan and his co-workers have demonstrated the synthesis of pillared-porous carbon nanosheet by using porous MgO sheets as template and pitch as carbon source, and the material exhibits the mesoporous structure with a pore size of 6–8 nm and a BET surface area of 883 m<sup>2</sup> g<sup>-1</sup>.<sup>7</sup> Except for the individual template commonly implemented, our research group has recently developed a dual-template carbonization method for producing nitrogen-doped porous carbon, in which Zn(NO<sub>3</sub>)<sub>2</sub>·6H<sub>2</sub>O and Mg(NO<sub>3</sub>)<sub>2</sub>·6H<sub>2</sub>O serve as double template. It can efficiently give rise to the formation of nanoporous carbon materials possessing high BET surface area of 1518 m<sup>2</sup> g<sup>-1</sup>, large pore volume of 4.27 cm<sup>3</sup> g<sup>-1</sup> and, consequently resulting in high specific capacitance of *ca.* 284.1 F g<sup>-1</sup>.<sup>8</sup> Up to now, further exploring more efficient template carbonization method for producing nanoporous carbon materials is still challenging and significant for material scientists.

However, the specific capacitance of nanoporous carbon as electrode materials (the specific capacitances of 120–350 F g<sup>-1</sup>) in the conventional electrolyte will be unable to fulfill commercial requirements in modern society.<sup>9</sup> In order to enhance specific capacitances of supercapacitors, introducing redox-additive into the electrolytes has been proved as a simple and effective way,<sup>10</sup> and the quick self-discharge reaction of active additive can greatly improve the capacitances of supercapacitors.<sup>11</sup> Till to now, the redox-additive can be primarily categorized into two species. Firstly, there has many reports regarding inorganic additives, such as K<sub>3</sub>Fe(CN)<sub>6</sub> or

<sup>a</sup>School of Chemistry and Chemical Engineering, Anhui Key Laboratory of Controllable Chemistry Reaction & Material Chemical Engineering, Hefei University of Technology, Hefei, Anhui 230009, P. R. China. E-mail: cxyhfut@gmail.com; Fax: +86-551-62901450; Tel: +86-551-62901450

<sup>b</sup>College of Chemistry & Chemical Engineering, Anhui Province Key Laboratory of Environment-friendly Polymer Materials, Anhui University, Hefei 230039, Anhui, P. R. China. E-mail: zhangzj0603@126.com

† Electronic supplementary information (ESI) available. See DOI: 10.1039/c5ra11187k

‡ These authors contribute to this work equally.

$\text{K}_4\text{Fe}(\text{CN})_6$ ,<sup>12</sup>  $\text{Na}_2\text{S}$  and  $\text{S}$  powder,<sup>13</sup>  $\text{CuSO}_4$ .<sup>11</sup> Furthermore, Senthikumar *et al.* have researched the improvement of specific capacitance by utilizing the mixed redox-electrolyte of  $\text{KI}$  ( $0.08 \text{ mol L}^{-1}$ ) and  $\text{H}_2\text{SO}_4$  ( $1 \text{ mol L}^{-1}$ ). The redox reagents of  $3\text{I}^-/\text{I}_3^-$ ,  $2\text{I}^-/\text{I}_2$ ,  $2\text{I}_3^-/3\text{I}_2$  and  $\text{I}_2/2\text{IO}_3^-$  can produce redox reactions at the electrolyte/electrode interface, consequently resulting in high specific capacitance of *ca.*  $912 \text{ F g}^{-1}$ .<sup>14</sup> Secondly, other kinds of organic redox-additives were also adopted, such as indigo carmine,<sup>15</sup> methylene blue,<sup>16</sup> *m*-phenylenediamine,<sup>17</sup> hydroquinone/quinine.<sup>18,19</sup> For instance, the mixed redox-electrolyte of alkali ( $\text{KOH}$ ) and organo-redox additive (*p*-phenylenediamine, PPD) has largely improved the specific capacitance of activated carbon based supercapacitor, consequently resulting in high specific capacitance of *ca.*  $605.2 \text{ F g}^{-1}$  in the mixed electrolyte (PPD +  $\text{KOH}$  electrolyte).<sup>20</sup> Markedly, the redox-additive can greatly enhance the specific capacitance capability of supercapacitors, because of the supernumerary pseudocapacitance of the fast electron transfer/proton transfer and reversible Faradic reaction in the mixed electrolyte.<sup>17</sup> Hence, the redox-additive electrolyte will have wide range of applications in supercapacitors. Nevertheless, the effect of redox additives in  $\text{KOH}$  electrolyte on electrochemical performances of templated carbon materials still needs to be illustrated in depth.

In this work, we demonstrate a template carbonization method to produce nanoporous carbon materials with hierarchical porosities, using potassium citrate (or gelatin) and  $\text{Mg}(\text{OH})_2$  as precursors. The impacts of the mass ratio of potassium citrate (or gelatin) and  $\text{Mg}(\text{OH})_2$ , as well as the dosage of PPD in  $\text{KOH}$  electrolyte on the structures and electrochemical behaviors of templated carbon materials were emphatically

investigated. The electrochemical performance of the samples was studied by a three-electrode system, utilizing mixed electrolyte of  $6 \text{ mol L}^{-1}$   $\text{KOH}$  and different amount of PPD.

## 2. Experiment

In present work, the potassium citrate (or gelatin) and  $\text{Mg}(\text{OH})_2$  have been converted into nanoporous carbon materials by a straightforward template carbonization method. The mass ratios of potassium citrate and  $\text{Mg}(\text{OH})_2$  were designated as 1 : 0 (without  $\text{Mg}(\text{OH})_2$ ), 3 : 1, and 5 : 1, respectively, which result in the formation of the P-blank/3 : 1/5 : 1 samples. As for the case of gelatin and  $\text{Mg}(\text{OH})_2$ , their mass ratios were designated as 1 : 1, 2 : 1, and 3 : 1, respectively, leading to the occurrence of the G-1 : 1/2 : 1/3 : 1 samples. Next, in order to further improve the electrochemical performances of these carbon samples, certain amounts of PPD additive as 5, 10, and  $15 \text{ mmol L}^{-1}$  were introduced in the  $6 \text{ mol L}^{-1}$   $\text{KOH}$ , forming the mixed electrolyte, which is anticipated to greatly modulate the electrochemical performances. The overall template carbonization method for producing nanoporous carbon materials, as well as the unit structures of potassium citrate and gelatin, is briefly depicted in Fig. 1.

### 2.1 Typical template carbonization method for nanoporous carbon materials

**Preparation of the P-3 : 1 sample.** Potassium citrate and  $\text{Mg}(\text{OH})_2$  powder with a mass ratio of 3 : 1 were first mixed and pulverized. The mixture was heated to  $800^\circ\text{C}$  at a rate of  $4^\circ\text{C min}^{-1}$  within a  $\text{N}_2$  flow for 2 h. After cooling down to room temperature, the black product was ground into powder and

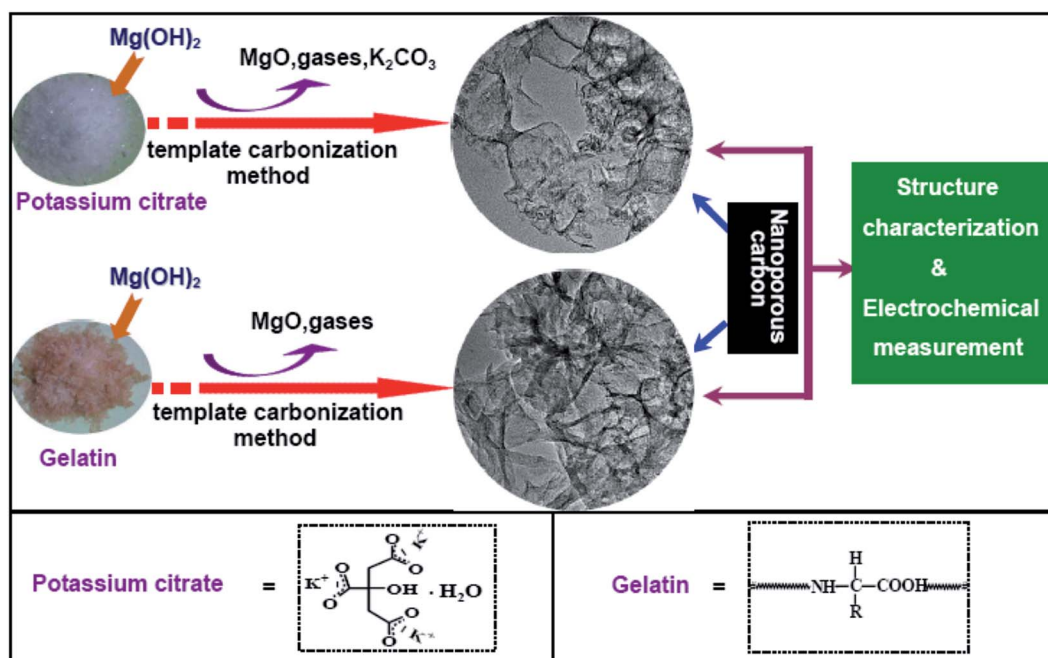


Fig. 1 Schematic illustration for producing nanoporous carbon materials derived from potassium citrate and gelatin by a  $\text{Mg}(\text{OH})_2$ -assisted template carbonization method (the above section), as well as the unit structures of potassium citrate and gelatin (the below section).

immersed in 1.0 mol L<sup>-1</sup> HCl solution to remove soluble/insoluble impurities. The product was washed with plenty of deionized water and ethanol till the filtrate became neutral and then dried overnight at 110 °C. Finally, the P-3 : 1 sample was acquired.

**Preparation of the G-1 : 1 sample.** Gelatin and Mg(OH)<sub>2</sub> powder with a mass ratio of 1 : 1 were added into apposite deionized water, and then were stirred at 80 °C by the magnetic stirrers. Finally, the viscous mixture was dried at 80 °C for 4 h to acquire the gel as precursor. The following carbonization and post-processing steps are similar to those of the P-3 : 1 sample, and the finally obtained carbon sample is named as G-1 : 1.

## 2.2 Structure characterization

High-resolution transmission electron microscope (HRTEM) images and selected area electron diffraction (SAED) patterns were performed with a JEM-2100F unit. The samples for HRTEM were prepared by ultrasonic dispersing the powder products in ethanol, which were then deposited and dried on a holey carbon film on a copper grid. The specific surface area (*S*<sub>BET</sub>) and pore structure of the carbon samples were determined by N<sub>2</sub> adsorption-desorption isotherms at 77 K (Quantachrome Autosorb-iQ) after being vacuum-dried at 150 °C overnight. The specific surface areas were calculated by the BET (Brunauer-Emmett-Teller) method. Cumulative pore volume and pore size distribution were calculated by using a slit/cylindrical nonlocal density functional theory (NLDFT) model. Powder X-ray diffraction (XRD) patterns were recorded on a Rigaku D/MAX2500V diffractometer using Cu Kα radiation (40 kV and 40 mA) at a scan rate of 2 deg min<sup>-1</sup>. Raman spectra were recorded at ambient temperature on a Spex 1403 Raman spectrometer with an argon-ion laser at an excitation wavelength of 514.5 nm. X-ray photoelectron spectra (XPS) were obtained on a VG ESCALAB MK II X-ray photoelectron spectrometer with an exciting source of Mg Kα (1253.6 eV).

## 2.3 Electrochemical measurements

The homogeneous slurry of 80 wt% as-prepared carbon materials (~4 mg), 5 wt% polytetrafluoroethylene (PTFE) binder, and 15 wt% graphite was combined using a few drops of 95% ethanol as solvent. Then, the working electrodes were fabricated by pressing the homogeneous slurry on a regular nickel form (1 cm × 1 cm) and dried at 110 °C for 12 h under vacuum oven. The redox-electrolyte was prepared by introducing different amount of PPD into the 6 mol L<sup>-1</sup> KOH, and then flushing with Ar flow for 2 h, so we can gain a sequence of redox-electrolyte. The three electrode system was performed in mixed aqueous electrolyte (6 mol L<sup>-1</sup> KOH and different amount of PPD) and the conventional 6 mol L<sup>-1</sup> KOH electrolyte with platinum foil (6 cm<sup>2</sup>) and saturated calomel electrode (SCE) electrodes as counter and reference electrodes, respectively. All the electrochemical measurements were carried out by an electrochemical workstation (CHI 660D). The procedures are briefly displayed as follows: cyclic voltammetry (CV) tests of the three-electrode system were performed in a voltage wide range of -1 to 0 V. Galvanostatic charge-discharge (GCD) was investigated in the same potential range at the current densities ranging from 2 to

40 A g<sup>-1</sup>. Electrochemical impedance spectroscopy (EIS) investigations were also carried out in the frequency range from 100 kHz to 0.01 Hz at open circuit potential with an ac perturbation of 5 mV. Before electrochemical measurements, the as-prepared electrodes were stabilized by using the CV at a scan rate of 100 mV s<sup>-1</sup> for about 12 cycles.

Specific capacitances derived from GCD measurements in a three-electrode cell can be obtained as the equation:

$$C = \frac{I\Delta t}{m\Delta V}$$

where *I* (A) is the constant current and *m* (g) is the mass of active materials loaded in the working electrode, Δ*t* (s) is the discharge time and Δ*V* (V) is the voltage change during the discharge process, *C* (F g<sup>-1</sup>) is the specific capacitance. The energy and power densities are calculated based on the equation, which is given in ESI† section.

## 3. Results and discussion

HRTEM was employed to intuitively depict the microstructure and morphology of the acquired P-3 : 1 sample. The legible HRTEM images (Fig. 2a and b) of the P-3 : 1 sample display plenty of nanoporous structures, which favor for the rapid diffusion of multiple electrolyte ions. Moreover, the SAED pattern (the inset of Fig. 2b) with vague diffraction rings explicitly indicates that the P-3 : 1 sample has a particular non-crystal character.

Further information about the textural porosities of the P-3 : 1 sample was investigated by N<sub>2</sub> adsorption-desorption at 77 K, and the N<sub>2</sub> adsorption-desorption isotherm exhibits the characteristics of type IV (according to the IUPAC classification), as indicated in Fig. 2c. In detail, a small increase is shown at low relative pressure, and the next slow rise of isotherm appears at medium relative pressure with the un conspicuous hysteresis loop, while the isotherm rise at the relative pressure is close to 1.0 points, indicating the co-existence of micropores, mesopores, and macropores in the P-3 : 1 sample.<sup>21</sup> Furthermore, the BET surface area, total pore volume, and average pore diameter can reach to 1894.7 m<sup>2</sup> g<sup>-1</sup>, 2.27 cm<sup>3</sup> g<sup>-1</sup>, and 4.79 nm, respectively. Besides, the cumulative pore volume and pore-size distribution curves are achieved by utilizing a slit/cylindrical NLDFT model.<sup>22</sup> Fig. 2d reveals some obvious pore width distribution peaks distributed in the range of 0–5 nm, which well match with the average pore diameter (4.79 nm) of the P-3 : 1 sample. The results reveal that the carbon sample contains hierarchical nanoporous structures, which are primarily derived from the decomposed products of potassium citrate and Mg(OH)<sub>2</sub>.<sup>23,24</sup>

XRD and Raman analysis techniques were further used to analyze the phase, crystallinity, and composition of the P-3 : 1 sample. Fig. 3a reveals the XRD pattern in the wide-angle range of 3–90° and an obvious diffraction peak centered at around 23.3° pertains to a representative (002) crystal plane of standard hexagonal graphite. Besides, the broad diffraction peak and the largely shifted from (002) plane of the standard hexagonal graphite (2θ = 26.6°) collectively demonstrate the amorphous



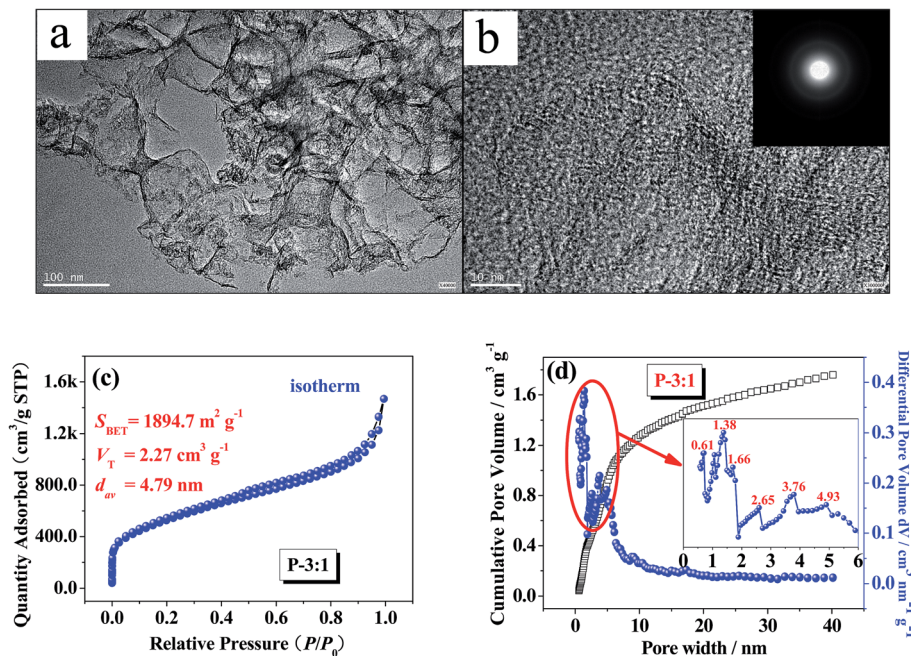


Fig. 2 The P-3 : 1 sample: (a and b) HRTEM images as well as the magnified SAED pattern (the insets); (c) N<sub>2</sub> adsorption–desorption isotherm; (d) cumulative pore volume and pore size distribution curves (estimated by using a slit/cylindrical NLDFT model).

state of the P-3 : 1 sample. Also, the largely expansion of inter-layers between (002) planes of the P-3 : 1 sample has been approved based on the Bragg equation ( $2d \sin \theta = \lambda$ ).<sup>25</sup> The amorphous nature of the P-3 : 1 sample is further affirmed by Raman spectra (the inset of Fig. 3a). The broad D-band ( $\sim 1354.3 \text{ cm}^{-1}$ ) situated in the low wavenumbers region corresponds to the disordered structures, and the wide G-band ( $\sim 1592.3 \text{ cm}^{-1}$ ) located at high wavenumbers area is attributed to the graphitic characteristic.<sup>26</sup> The value of  $I_D/I_G$  that is achieved by the integral area ratio of the D- and G-band is calculated as 2.75, which confirms the low crystallization level of the P-3 : 1 sample again,<sup>27</sup> which well accords with the HRTEM results mentioned above.

The composition of the P-3 : 1 sample and functional groups on the nanoporous carbon surface have been analyzed by XPS. In the XPS survey (Fig. 3b), two primary peaks directly corresponding to the C1s and O1s peaks occur. Also, the percentage contents of carbon and oxygen are displayed by a histogram (the inset of Fig. 3b). Furthermore, Fig. 3c reveals the C1s spectra (284–299 eV) with three distinguishing peaks, which are analyzed as follows: the main peak on  $(284.5 \pm 0.1) \text{ eV}$  corresponds to  $\text{C}=\text{C}$  bonds (non-functionalised  $\text{sp}^2 \text{ C}$ ),<sup>28</sup> and the peak at  $(285.11\text{--}285.5) \text{ eV}$  is induced by the  $\text{sp}^3 \text{ C-C}$  bonds. As for the peak at around 287.5 eV, it is attributed to  $\text{sp}^3$  carbon atoms.<sup>29</sup> Similarly, three typical peaks have been acquired by deconvoluting the O1s spectra (Fig. 3d), which demonstrate the oxygen-containing functional group may consist of  $\text{O}=\text{C}$  ( $531.65\text{--}531.94 \text{ eV}$ ),<sup>30</sup> carbonyl oxygen in the ester ( $532.3 \pm 0.3 \text{ eV}$ ), and  $\text{C-O-C}\equiv$  ( $532.3 \pm 0.3 \text{ eV}$ ).<sup>28</sup> Furthermore, the percentage contents of carbon and oxygen species are described by concise histograms (the insets of Fig. 3c and d).

To evaluate the feasibility of the present carbon samples as supercapacitor electrode materials, the electrochemical performance were analyzed, as deeply presented in the ESI section (Fig. S1 and 2†). By all appearance, the P-3 : 1 sample has the optimized electrochemical performance in traditional  $6 \text{ mol L}^{-1}$  KOH electrolyte. On the other hand, in order to further analyze the changes of electrochemical properties, a three-electrode system using the mixed electrolytes of  $6 \text{ mol L}^{-1}$  KOH with different amount of PPD of 5, 10, and  $15 \text{ mmol L}^{-1}$ , respectively, acting as redox additive were utilized for the electrochemical tests, along with the potential window of  $-1.0$  to  $0.0 \text{ V}$ . These mixed electrolytes are marked as P-3 : 1-5, P-3 : 1-10 and P-3 : 1-15, respectively.

Fig. 4a displays the contrast CV curves of the P-3 : 1, P-3 : 1-5/10/15 samples. In the case of the P-3 : 1 sample when measured in conventional  $6 \text{ mol L}^{-1}$  KOH electrolyte, the CV curve exhibits the quasi-rectangular shape without obvious redox peaks, revealing that the predominant contribution is derived from electrochemical double layer capacitor (EDLC).<sup>31</sup> By contrast, while adding different concentrations of PPD into the KOH electrolyte, the CV curves of the P-3 : 1-5/10/15 samples suddenly emerge a pair of symmetric and obvious redox peaks. Concretely, the reductive peaks are located at the peak potential ranging from  $-0.6 \text{ V}$  to  $-0.5 \text{ V}$ , and the oxidative peaks situate in the peak potential of  $-0.2 \text{ V}$  to  $-0.1 \text{ V}$ . Those results reveal the joint contribution of the EDLC and the excellent pseudo-capacitance performances from redox-additive (PPD) electrolyte. Specifically, these redox peaks in Fig. 4a are derived from the rapid redox-reaction of the redox couple (*p*-phenylenediamine/*p*-phenylenediimine),<sup>32</sup> and the reaction mechanism will be illustrated in the following section. Besides, the peak

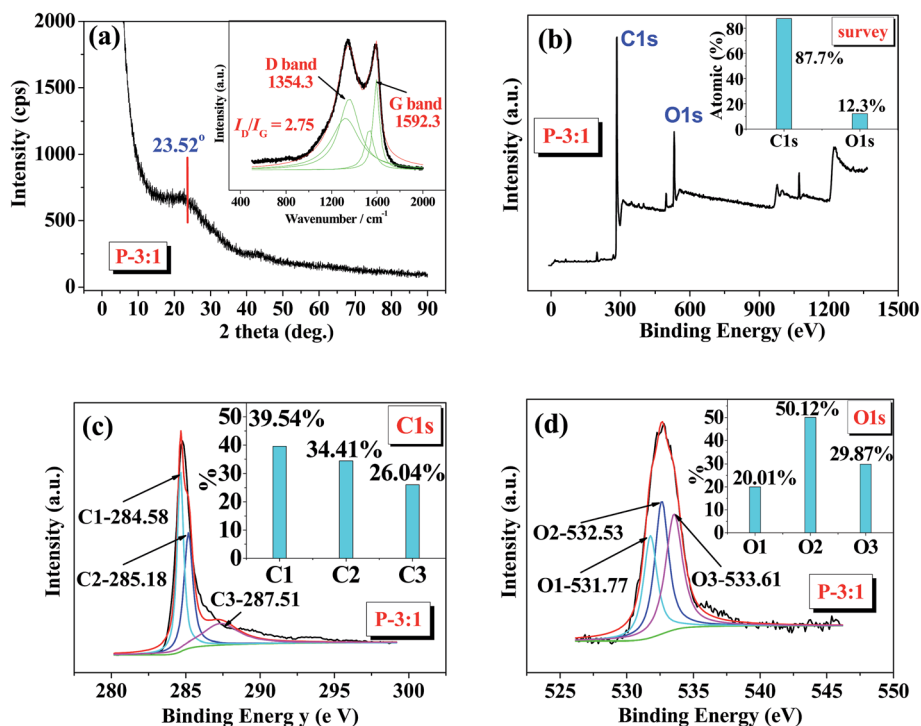


Fig. 3 The P-3 : 1 sample: (a) XRD pattern as well as the Raman spectrum (the insets); (b) survey (the insets are summary of carbon/oxygen contents); (c and d) C1s, O1s spectra with deconvoluted peaks (the insets are contents of different carbon, oxygen species).

intensities of redox peaks gradually enhance with the increasing concentration of PPD from 5 to 10, and 15 mmol L<sup>-1</sup>.

In order to further analyze the electrochemical performance of the P-3 : 1 sample, the GCD curves are measured at a current density of 2 A g<sup>-1</sup> in the potential window ranging from -1.0 V to 0 V, as exhibited in Fig. 4b. It is found that the discharging times visibly enlarge with the addition of different amount of PPD into the electrolyte. As is well seen, the GCD curve of the P-3 : 1 sample is close to the symmetric triangle, suggesting the main contribution from EDLC and the excellent reversibility. On the other side, the GCD curves of the P-3 : 1-5/10/15 exhibit conspicuous charging and discharging platforms, indicating that the redox reactions of the PPD occur in the process of galvanostatic charge-discharge (GCD). In consequence, the discharging time can be greatly enhanced by using the PPD as the redox-additive, which can produce redox-reaction on the surface of the pores within the carbon matrix. Furthermore, Fig. 4c provides the specific capacitance data at the current density ranging from 2 A g<sup>-1</sup> to 10 A g<sup>-1</sup>, and all curves exhibit slight decline with the gradual increase of current density, in which the ions diffusion rate is limited at higher current density.<sup>33</sup> Moreover, it is indicated that the specific capacitances have greatly improved by introducing the PPD into the 6 mol L<sup>-1</sup> electrolyte, especially the unexceptionable mixed electrolyte of the case of P-3 : 1-15 when designating the PPD concentration at 15 mmol L<sup>-1</sup>. As a result, at a current density of 2 A g<sup>-1</sup>, the specific capacitances can reach up to 579.2, 712.8 and 852.3 F g<sup>-1</sup>, respectively, in cases of the P-3 : 1-5/10/15 samples, which are greatly higher than that of 325 F g<sup>-1</sup> for

the case of pristine P-3 : 1 sample when measured at conventional electrolyte (6 mol L<sup>-1</sup> KOH).

The electrochemical impedance spectroscopy (EIS) technology is also utilized to evaluate the capacitive property and electrode conductivity of carbon-based electrode in the present system, and the resulting Nyquist plots are illustrated in Fig. 4d. Apparently, three main portions of the Nyquist plots are indicated as follows: the semi-circle loop locates at the higher frequencies region, an oblique line with an angle of 45° in the middle frequency region called the Warburg resistance, and the typical slant line in the low frequency district.<sup>34,35</sup> We can find that the P-3 : 1-15 sample delivers the most excellent electrochemical impedance property by using the mixed-electrolyte. Specifically, the short diameter of semi-circle is related to the low charge-transfer resistance in the interface of electrode materials, which comes from the fast redox-reaction of the *p*-phenylenediamine/*p*-phenylenediimine (PPD/PDI). In addition, the sloping line without obvious vertical feature locates at low frequency region is attributed to the hierarchical porosities of nanoporous carbon materials.<sup>36</sup> Hence, the high BET surface area, favorable pore-size distribution, and the fast redox-reaction of the PPD can be concluded as the crucial conditions for the excellent performance of the electrochemical impedance.

The feasible redox-reaction mechanism is illustrated in Fig. 4e. Concretely, the reductive and oxidative peaks of the CV curves are correlative with the fast redox-reaction of the PPD, in other words, the redox couple (PPD/PDI) consisting in the mixed electrolyte.<sup>32</sup> In the reverse scan, the oxidation state (PDI)

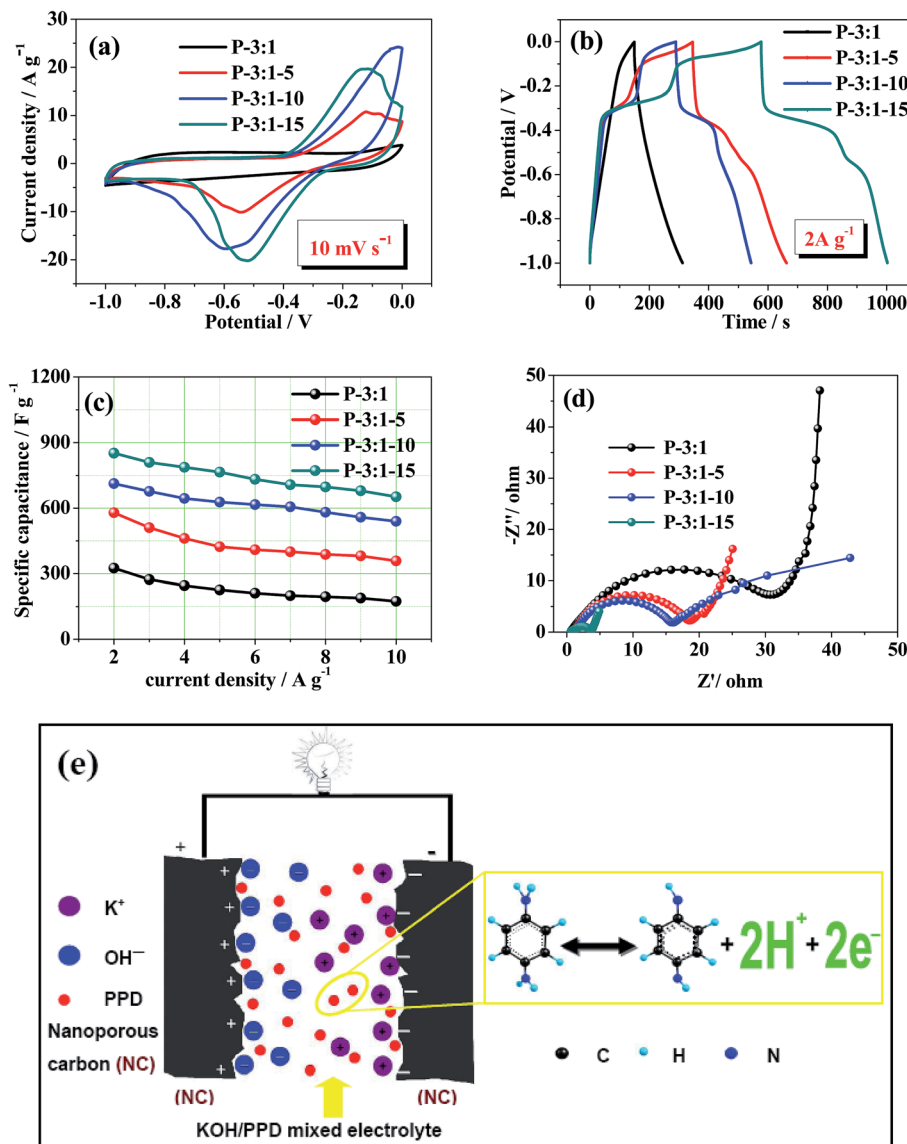


Fig. 4 The P-3 : 1, P-3 : 1-5/10/15 samples measured in a three-electrode system using mixed electrolyte (6 mol L<sup>-1</sup> KOH with different amount of PPD acting as redox additive): (a) CV curves at a scan rate of 10 mV s<sup>-1</sup>; (b) GCD curves at a current density of 2 A g<sup>-1</sup>; (c) specific capacitances calculated from GCD curves; (d) Nyquist plots; (e) electrochemical reaction mechanism of redox additive electrolyte of PPD in the mixed electrolyte.

can receive 2-electrons and 2-protons, and thus results in the reductive peak. And in the positive scan, the reduction state (PPD) can lose 2-electrons and 2-protons, and thus generates the oxidative peak. Furthermore, the clear charging-discharging platforms of GCD curves also support the viewpoint. Ultimately, these rapid transfer reactions of the electrons and protons in the interface between the electrode and mixed-electrolyte will lead to the improvement of electrochemical behaviors.

Based on the above discussion, it is clearly seen that the P-3 : 1-15 sample displays the most excellent electrochemical behaviors. It has been further researched and the relevant results are presented in Fig. 5. Fig. 5a displays the CV curves at a variety of scan rates (5–400 mV s<sup>-1</sup>), and the broad and obvious redox peaks appear at low scan rates (5–20 mV s<sup>-1</sup>). In general,

the electrode reactions are heterogeneous and take place in the interfacial region between electrode materials and electrolyte. While the interaction gradually weakens with the increase of scan rates (50–400 mV s<sup>-1</sup>), and the CV curves become more distorted, that is to say, a large number of ions have not enough transition time to reach the surface of the electrode.<sup>37</sup> Furthermore, the GCD curves measured at a series of current density (2–10 A g<sup>-1</sup>) are described in Fig. 5b. Obviously, all GCD curves have apparent charging-discharging platforms attributed to the effective redox-reaction, which are in good accordance with the CV results mentioned above.

Concerning the cycling stability of the P-3 : 1-15 sample, which is a pregnant performance of the as-prepared carbon-based electrode, and it is measured at a higher current

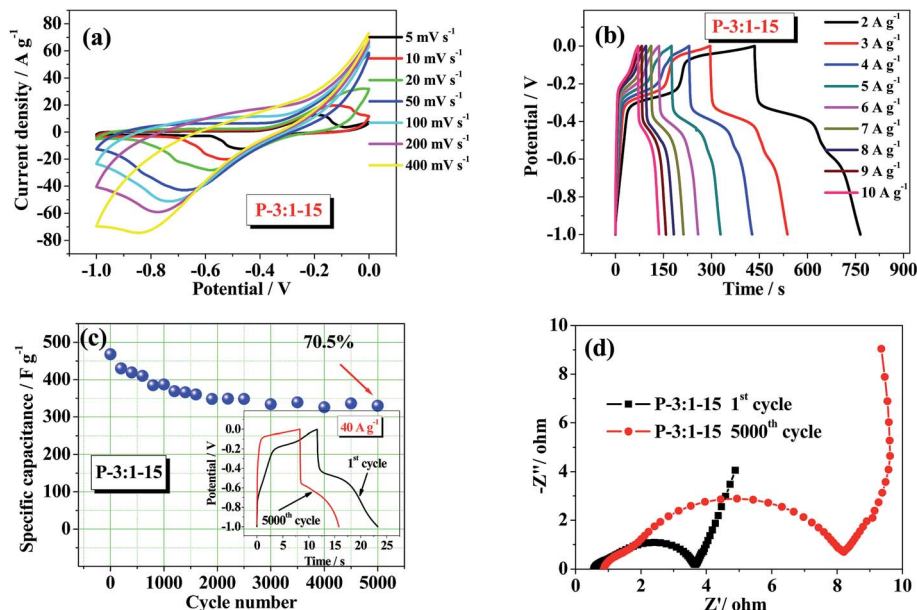


Fig. 5 The P-3 : 1-15 sample measured in a three-electrode system using mixed electrolyte (6 mol L<sup>-1</sup> KOH and 15 mmol L<sup>-1</sup> PPD): (a) CV curves at different scan rates; (b) GCD curves at different current densities; (c) cycling stability measured at 40 A g<sup>-1</sup> as well as GCD curves before/after 5000 cycles cycling stability measured at 40 A g<sup>-1</sup> (the insets); (d) Nyquist plots before/after 5000 cycles.

density of 40 A g<sup>-1</sup> in the mixed electrolyte, as shown in Fig. 5c. Obviously, the specific capacitance value can maintain as high as 330.2 F g<sup>-1</sup> after 5000 cycles of charge–discharge process, compared with the initial one of 468 F g<sup>-1</sup>. In other words, the

pseudocapacitance derived from redox-reaction of the PPD and the EDLC dated from the higher BET specific surface area and large pore volume of the P-3 : 1 sample are quite stable. In addition, the 1<sup>st</sup> and 5000<sup>th</sup> GCD curves at a current density of

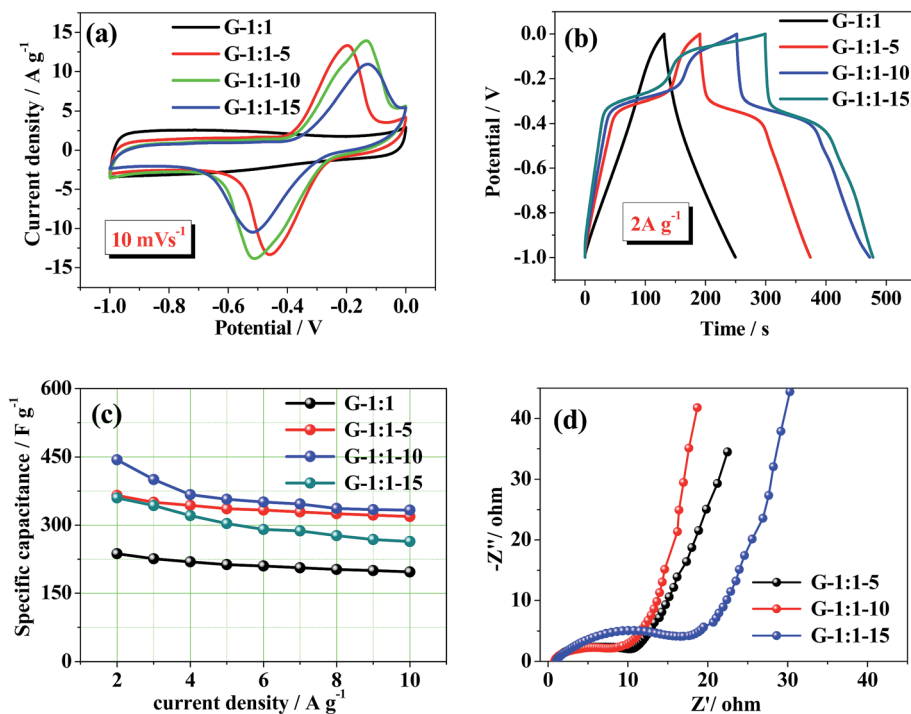


Fig. 6 The G-1 : 1, G-1 : 1-5/10/15 samples measured in a three-electrode system using mixed electrolyte (6 mol L<sup>-1</sup> KOH with different amount of PPD acting as redox additive): (a) CV curves at a scan rate of 10 mV s<sup>-1</sup>; (b) GCD curves at a current density of 2 A g<sup>-1</sup>; (c) specific capacitances calculated from GCD curves; (d) Nyquist plots.



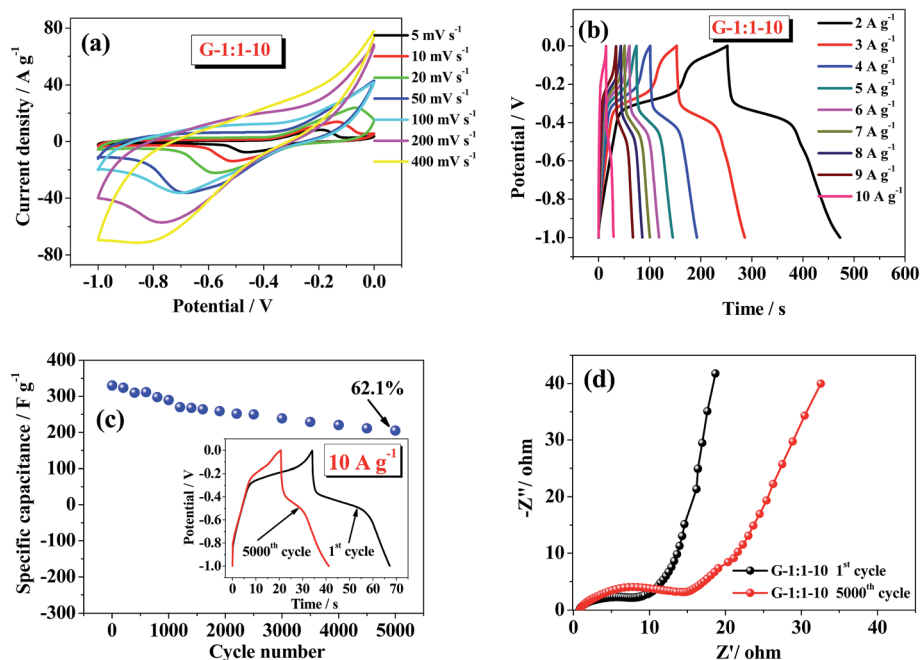


Fig. 7 The G-1 : 1-10 sample measured in a three-electrode system using mixed electrolyte (6 mol L<sup>-1</sup> KOH and 10 mmol L<sup>-1</sup> PPD): (a) CV curves at different scan rates; (b) GCD curves at different current densities; (c) cycling stability measured at 10 A g<sup>-1</sup> as well as GCD curves before/after 5000 cycles cycling stability measured at 10 A g<sup>-1</sup> (the insets); (d) Nyquist plots before/after 5000 cycles.

40 A g<sup>-1</sup> are demonstrated in the inset of Fig. 5c. In order to fully analyze the Nyquist plots of the carbon-based electrodes, the Nyquist plots before/after 5000 cycles are illustrated in Fig. 5d. Apparently, with the increase of cycling time, the diameter of semi-circle at high frequency regions has become larger in length, which is correlative with the resistance augments of the carbon-based electrode.

### The synthesis expansion to the other system of gelatin and Mg(OH)<sub>2</sub>

In order to across-the-board analyze the changes of electrochemical performance by utilizing diverse carbon sample as electrode, so the synthesis precursor was extended to gelatin and Mg(OH)<sub>2</sub>. The as-prepared nitrogen-doped nanoporous carbon materials (G-1 : 1/2 : 1/3 : 1 samples) were characterized by means of several techniques such as TEM, BET, XRD, Raman, and XPS (the detailed results have been shown in Fig. S3 and 4†). Besides, the electrochemical performance was also studied by utilizing a three-electrode system using the electrolyte of 6 mol L<sup>-1</sup> KOH, along with the potential window of -1.0 to 0.0 V (detailed data are exhibited in Fig. S5 and 6†). Furthermore, the electrochemical performance of the optimal G-1 : 1 sample was measured in the conventional electrolyte of 6 mol L<sup>-1</sup> KOH. Moreover, it was further analyzed by utilizing a three-electrode system using the mixed electrolyte (6 mol L<sup>-1</sup> KOH + 5/10/15 mmol L<sup>-1</sup> PPD), denoted as the G-1 : 1-5, G-1 : 1-10, and G-1 : 1-15 samples, respectively.

Fig. 6a shows the quasi-rectangular CV curve of the G-1 : 1 sample at a scan rate of 10 mV s<sup>-1</sup> without adding the redox-additive (PPD) into the electrolyte, while the CV curves of the

G-1 : 1-5/10/15 samples have apparent redox-peaks with the increase of PPD, which are derived from the redox reaction of the PPD. Furthermore, the GCD curves are measured at a current density of 2 A g<sup>-1</sup>, and all results toward the G-1 : 1, G-1 : 1-5/10/15 samples are displayed in Fig. 6b. It is very clearly seen that the discharging time has been greatly enlarged when the redox-additive (PPD) was introduced into the 6 mol L<sup>-1</sup> KOH electrolyte. Moreover, the charging and discharging platforms of the GCD curves can also be observed. On the whole, all trends of the CV and GCD of the G-1 : 1, G-1 : 1-5/10/15 samples well agree with those of the above P-3 : 1, P-3 : 1-5/10/15 samples.

Fig. 6c explicitly reveals the specific capacitances at the various current density (2–10 A g<sup>-1</sup>), and we can find that it gradually decreases with the increase of current density. On the other hand, the specific capacitance has greatly enhanced with the increase of concentration of the PPD from 5 to 10, and 15 mmol L<sup>-1</sup>. Obviously, the preeminent mixed electrolyte is a 6 mol L<sup>-1</sup> KOH aqueous electrolyte containing the 10 mmol L<sup>-1</sup> PPD, and the specific capacitance of the G-1 : 1-10 sample at a current density of 2 A g<sup>-1</sup> can reach up to 444.5 F g<sup>-1</sup>, much higher than that (236.8 F g<sup>-1</sup>) of the G-1 : 1 sample. By contrast, the P-3 : 1-15 sample can reach up to 852.3 F g<sup>-1</sup> at an identical current density of 2 A g<sup>-1</sup>, which are mostly due to the higher BET specific area (1894.7 m<sup>2</sup> g<sup>-1</sup>) and the large total pore volume (2.27 cm<sup>3</sup> g<sup>-1</sup>). Despite the nitrogen content of the G-1 : 1 carbon sample can reach up to 7.76% (Fig. S4c†), which can enhance the electrochemical characteristics,<sup>38</sup> but the BET specific area is only 965.4 m<sup>2</sup> g<sup>-1</sup> and the pore volume of 1.42 cm<sup>3</sup> g<sup>-1</sup> (Fig. S3c†). As a result, the P-3 : 1-15 sample



delivers much better electrochemical performance than that of the G-1 : 1-10 sample.

In order to identify the intrinsic interaction between the redox-additive and the surface of electrode, the electrical impedance spectroscopy (EIS) of the G-1 : 1-5/10/15 samples at room temperature in the frequency ranging from 0.01 to  $10^5$  Hz has been measured, as exhibited in Fig. 6d. It is well revealed that the carbon-based electrode has good performance of electrical impedance in the moderate concentration ( $10 \text{ mmol L}^{-1}$ ) of the PPD, which may due to the low concentration of the PPD ( $5 \text{ mmol L}^{-1}$ ) is not able to supply enough electrons or/and ions for enhancing the conductivity of the new system, while higher concentration of the PPD ( $15 \text{ mmol L}^{-1}$ ), which is adverse to the transfer of electrons and various ions.

Fig. 7a illustrates CV curves of the G-1 : 1-10 sample at different scan rates ( $5\text{--}400 \text{ mV s}^{-1}$ ). Moreover, we can discern that it exhibits obvious CV redox peaks at low scan rates such as 5, 10, and  $20 \text{ mV s}^{-1}$ , but the CV curves gradually become distorted with the increase of scan rates. This is probably due to the interaction between the electrolyte and the carbon-based electrode diminishing gradually.<sup>39</sup> Fig. 7b shows the GCD curves at the different current densities ranging from 2 to  $10 \text{ A g}^{-1}$ . All GCD curves have obvious charging and discharging platforms, clearly derived from the redox reaction of the PPD. The long-term charging–discharging process of the G-1 : 1-10 sample at a current density of  $10 \text{ A g}^{-1}$  was measured, as shown in Fig. 7c. It is found that the capacitance retention still can reach to 62.1% after 5000 cycles. Moreover, the GCD curves (1<sup>st</sup> and 5000<sup>th</sup> cycles) at a current density of  $10 \text{ A g}^{-1}$  are also exhibited in the inset of Fig. 7c. The Nyquist plots before/after 5000 cycles are displayed in Fig. 7d. Obviously, the diameter of semi-circle after 5000 cycles is larger than the original diameter and the line at low frequency much deviation from the vertical line, demonstrating that the resistance of the G-1 : 1-10 sample after 5000 cycles slightly increases.

## 4. Conclusions

The P-3 : 1 sample with higher specific surface and the G-1 : 1 sample with high nitrogen content have been produced *via* template carbonization method, and the as-produced samples have excellent electrochemical characteristics. To further enhance electrochemical performance, we have introduced PPD into the conventional  $6 \text{ mol L}^{-1}$  KOH electrolyte.

In summary, the scientific advantages for this new system are particularized as follows:

- (1) The template carbonization method is a simple and valid method for producing nanoporous carbon materials, especially without any physical/chemical activation process;
- (2) The PPD as a kind of redox additive in the mixed electrolyte can generate quick and reversible redox-reaction with the 2-electrons and 2-protons transfer;
- (3) The electrochemical performance of the supercapacitor electrode has been greatly improved by combining EDLC and the excellent pseudocapacitance performances from redox-additive (PPD) electrolyte.

## Acknowledgements

This work was financially supported by the National Natural Science Foundation of China (21101052). Dr Zhong Jie Zhang thanks the financial support from Anhui Provincial Natural Science Foundation (1508085QE104).

## References

- 1 H. Nishihara and T. Kyotani, *Adv. Mater.*, 2012, **24**, 4473–4498.
- 2 A. H. Farmahinia and S. K. Bhatia, *Mol. Simul.*, 2015, **41**, 432–445.
- 3 G. P. Wang, L. Zhang and J. J. Zhang, *Chem. Soc. Rev.*, 2012, **41**, 797–828.
- 4 Y. P. Zhai, Y. Q. Dou, D. Y. Zhao, P. F. Fulvio, R. T. Mayes and S. Dai, *Adv. Mater.*, 2011, **23**, 4828–4850.
- 5 P. Simon and Y. Gogotsi, *Acc. Chem. Res.*, 2013, **46**, 1094–1103.
- 6 J. Balach, L. Tamborini, K. Sapag, D. F. Acevedo and C. A. Barbero, *Colloids Surf., A*, 2012, **415**, 343–348.
- 7 Z. J. Fan, Y. Liu, J. Yan, G. Q. Ning, Q. Wang, T. Wei, L. J. Zhi and F. Wei, *Adv. Energy Mater.*, 2012, **2**, 419–424.
- 8 X. Y. Chen, C. Chen, Z. J. Zhang and D. H. Xie, *J. Mater. Chem. A*, 2013, **1**, 10903–10911.
- 9 L. L. Zhang and X. S. Zhao, *Chem. Soc. Rev.*, 2009, **38**, 2520–2531.
- 10 G. Lota and G. Milczarek, *Electrochem. Commun.*, 2011, **13**, 470–473.
- 11 L. B. Chen, H. Bai, Z. F. Huang and L. Li, *Energy Environ. Sci.*, 2014, **7**, 1750–1759.
- 12 L. H. Su, X. G. Zhang, C. H. Mi, B. Gao and Y. Liu, *Phys. Chem. Chem. Phys.*, 2009, **11**, 2195–2202.
- 13 L. Qian, X. Q. Tian, L. Yang, J. F. Mao, H. Y. Yuan and D. Xiao, *RSC Adv.*, 2013, **3**, 1703–1708.
- 14 S. T. Senthilkumar, R. K. Selvan, Y. S. Lee and J. S. Melo, *J. Mater. Chem. A*, 2013, **1**, 1086–1095.
- 15 R. Silvia, G. Zoraida, B. Clara, G. Marcos, M. Rosa and S. Ricardo, *Electrochim. Acta*, 2011, **56**, 3401–3405.
- 16 R. Silvia, G. Marcos, M. Rosa, S. Ricardo and B. Clara, *Electrochim. Acta*, 2012, **83**, 241–246.
- 17 H. J. Yu, L. Q. Fan, J. H. Wu, Y. Z. Lin, M. L. Huang, J. M. Lin and L. Zhang, *RSC Adv.*, 2012, **2**, 6736–6740.
- 18 R. Silvia, G. Marcos, M. Rosa, S. Ricardo and B. Clara, *J. Phys. Chem. C*, 2011, **115**, 17606–17611.
- 19 S. Sathyamoorthi, V. Suryanarayanan and D. Velayutham, *J. Power Sources*, 2015, **274**, 1135–1139.
- 20 J. H. Wu, H. J. Yu, L. Q. Fan, G. G. Luo, J. M. Lin and M. L. Huang, *J. Mater. Chem.*, 2012, **22**, 19025–19030.
- 21 W. Xing, C. C. Huang, S. P. Zhuo, X. Yuan, G. Q. Wang, D. Hulicova-Jurcakova, Z. F. Yan and G. Q. Lu, *Carbon*, 2009, **47**, 1715–1722.
- 22 D. Portehault, C. Giordano, C. Gervais, I. Senkovska, S. Kaskel, C. Sanchez and M. Antonietti, *Adv. Funct. Mater.*, 2010, **20**, 1827–1833.
- 23 S. Marta and A. B. Fuertes, *ACS Nano*, 2014, **8**, 1963–1970.

- 24 J. Yan, Q. Wang, T. Wei, L. L. Jiang, M. L. Zhang, X. Y. Jing and Z. J. Fan, *ACS Nano*, 2014, **8**, 4720–4729.
- 25 Z. Q. Li, C. J. Lu, Z. P. Xia, Y. Zhou and Z. Luo, *Carbon*, 2007, **45**, 1686–1695.
- 26 R. J. Nemanich and S. A. Solin, *Phys. Rev. B: Condens. Matter Mater. Phys.*, 1979, **20**, 392–401.
- 27 F. Tuinstra and J. L. Koenig, *J. Chem. Phys.*, 1970, **53**, 1126–1130.
- 28 W. Z. Shen, Z. J. Li and Y. H. Liu, *Recent Pat. Chem. Eng.*, 2008, **1**, 27–40.
- 29 H. B. Wang, T. Maiyalagan and X. Wang, *ACS Catal.*, 2012, **2**, 781–794.
- 30 T. I. T. Okpalugo, P. Papakonstantinou, H. Murphy, J. McLaughlin and N. M. D. Brown, *Carbon*, 2005, **43**, 153–161.
- 31 B. Xua, F. Wu, Y. F. Su, G. P. Cao, S. Chen, Z. M. Zhou and Y. S. Yang, *Electrochim. Acta*, 2008, **53**, 7730–7735.
- 32 N. J. Ke, S. S. Lu and S. H. Cheng, *Electrochem. Commun.*, 2006, **8**, 1514–1520.
- 33 D. N. Futaba, K. Hata, T. Yamada, T. Hiraoka, Y. Hayamizu and Y. Kakudate, *Nat. Mater.*, 2006, **5**, 987–994.
- 34 M. D. Stoller, S. Park, Y. W. Zhu, J. An and R. S. Ruoff, *Nano Lett.*, 2008, **8**, 3498–3502.
- 35 Y. Wang, Z. Q. Shi, Y. Huang, Y. F. Ma, C. Y. Wang, M. M. Chen and Y. S. Chen, *J. Phys. Chem. C*, 2009, **113**, 13103–13107.
- 36 Z. Q. Niu, W. Y. Zhou, J. Chen, G. X. Feng, H. Li, W. J. Ma, J. Z. Li, H. B. Dong, Y. Ren, D. Zhao and S. S. Xie, *Energy Environ. Sci.*, 2011, **4**, 1440–1446.
- 37 J. Lahaye, G. Nanse, A. Bagreev and V. Strelko, *Carbon*, 1999, **37**, 585–590.
- 38 H. J. Denisa, A. M. Puziy, O. I. Poddubnaya, S. G. Fabian, J. M. D. Tascon and G. Q. Lu, *J. Am. Chem. Soc.*, 2009, **131**, 5026–5027.
- 39 X. R. Wen, D. S. Zhang, L. Y. Shi, T. T. Yan, H. Wang and J. P. Zhang, *J. Mater. Chem.*, 2012, **22**, 23835–23844.